Local Heat Transfer Dependency on Thermal Boundary Condition in Ribbed Cooling Channel Geometries

Beni Cukurel[1,2]
e-mail: bcukurel@technion.ac.il

Tony Arts
e-mail: arts@vki.ac.be

von Karman Institute for Fluid Dynamics,
Turbomachinery Department,
Chaussée de Waterloo, 72,
B-1640 Rhode-St-Genese, Belgium

The present study is geared toward quantifying the effects of imposed thermal boundary condition in cooling channel applications. In this regard, tests are conducted in a generic passage, with evenly distributed rib type perturbators at 90 deg, with a 30% passage blockage ratio and pitch-to-height ratio of 10. Uniform heat-flux is imposed on the external side of the slab which provides Biot number and solid-to-fluid thermal conductivity ratio around 1 and 600, respectively. Through infrared thermometry measurements over the wetted surface and via an energy balance within the solid, conjugate heat transfer coefficients are calculated over a single rib-pitch. The local heat extraction is demonstrated to be a strong function of the conduction effects, observed more dominantly in the rib vicinity. Moreover, the aero-thermal effects are investigated by comparing the findings with analogous aerodynamic literature, enabling heat transfer distributions to be associated with distinct flow structures. Furthermore, the results are contrasted with the iso-heat-flux wetted boundary condition test case. Neglecting the thermal boundary condition dependence, and thus the true thermal history of the boundary layer, is demonstrated to produce large errors in heat transfer predictions. [DOI: 10.1115/1.4024494]

Keywords: conjugate heat transfer, cooling channel, convection, infrared thermography, ribbed channel, thermal boundary condition

Introduction

Both numerical and experimental investigations of heat transfer enhancing cooling geometries should reproduce the thermal boundary conditions that reflect the application environment. Most studies do not address the influence of the thermal boundary condition. However, in case of large spatial thermal gradients and/or geometrical asperities, the wall temperature distribution's impact on heat transfer may be large. In purely convective models, where uniform temperature or uniform heat flux is imposed along the wetted surface, the thermal boundary condition is clearly not realistic. On the contrary, in the conjugate heat transfer case, where the effects of the solid domain conduction are coupled with the convection over the surface (i.e., the thermal history of the boundary layer is accurately modeled), no constraint is enforced at the solid-fluid interface, except thermal equilibrium and heat flux continuity. The methodology of conjugate heat transfer analysis presents the opportunity to accurately model the true heat transfer mechanisms.

The present research effort is devoted to a deeper understanding of the conjugate heat transfer phenomenon by conducting experiments toward fundamental understanding through generic cooling channel models. This study is among the few comparative heat transfer studies, confronting the results of a fully coupled conjugate investigation with purely convective iso-heat-flux boundary condition data, and exemplifies the pioneering experimental efforts to include the effects of conduction coupling in forced convection applications. In addition, the different heat transfer enhancement effects of various aerodynamic flow structures, as acquired by particle image velocimetry (PIV) experiments conducted a priori, are investigated.

In this regard, a uniform heat flux boundary condition is applied at the external side of a geometrically scaled test section model of a simplified turbine internal cooling channel, Fig. 1(*a*). The investigation focuses on surface heat flux calculations through local temperature measurements performed by infrared thermography. The heat flux distribution along the wetted side of the slab, computed from an energy balance within the metal domain, ultimately yields the Nusselt number distributions over the ribbed surface.

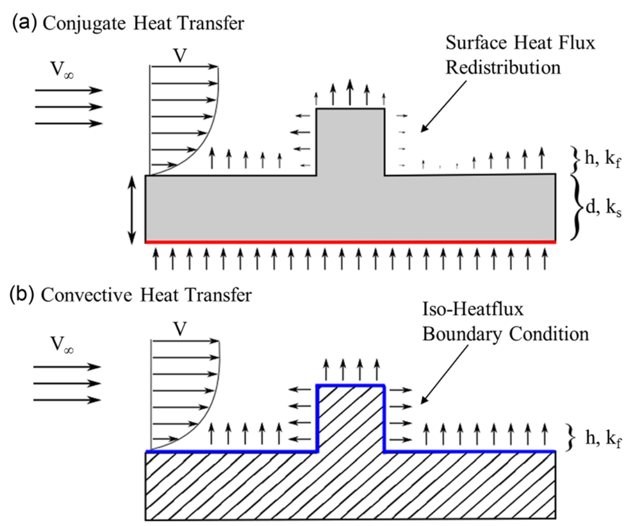

Fig. 1 Conjugate (*a*) versus convective (*b*) heat transfer

[1]Present address: The Turbo and Jet Engine Laboratory, Faculty of Aerospace Engineering, Technion, Israel Institute of Technology, Haifa 32000, Israel.
[2]Corresponding author.

Contributed by the Heat Transfer Division of ASME for publication in the Journal of Heat Transfer. Manuscript received April 17, 2012; final manuscript received January 17, 2013; published online September 11, 2013. Assoc. Editor: Roy E. Hogan.

Similarity Analysis

Considering the fluid flow along a nonadiabatic passage where convection-conduction coupled (conjugate) heat transfer phenomena takes place, making explicit use of the Buckingham-Pi theorem, the relation of the primary variables among each another can be reduced to a relation between the base quantities, yielding the dimensionless form

$$f(\mathrm{Re}, \mathrm{Pr}, \mathrm{Ec}, T_\infty/\Delta T, \mathrm{Nu}, K, \mathrm{Bi}) = 0 \quad (1)$$

where Ec, $T_\infty/\Delta T$, Nu, K, Bi are the Eckert number, the scaled relative bulk flow temperature, the Nusselt number, the solid-fluid thermal conductivity ratio, and the Biot number.

The relative bulk flow temperature, $T_\infty/\Delta T$, is experimentally found to have only a small influence and thus is neglected. This is a fair assumption when the physical properties of the fluid do not vary significantly with respect to temperature and small temperature differences [1]. The Eckert number is a measure of the viscous dissipation of the flow, arising in high-speed heat transfer problems. Especially for low speed applications, the relative importance of the kinetic energy with respect to the enthalpy is found to be very small, which largely reduces the influence of this dimensionless quantity. Moreover, for a given gas in a confined temperature range, the variation of Pr is negligible. Therefore, one can infer that a nondimensional temperature distribution in a scaled test facility of a geometrically similar internal cooling cavity proves to be aero-thermally similar, when Re, K, and Bi are maintained

$$\mathrm{Nu} = f(\mathrm{Re}, \mathrm{K}, \mathrm{Bi}) \quad (2)$$

Thus, for a conjugate problem with fixed geometric and aerodynamic constraints, the heat transfer depends not only on the local flow but also on the solid and air thermal conductivities, as well as on the thickness of the material, Fig. 1(*a*). In contrast, if the choice of the thermal boundary condition is assumed to have a negligible effect on the surface heat transfer, the convective problem would diminish its solid dependency, where Nu is only a function of Re, Fig. 1(*b*).

The intensity of the conjugate heat transfer effect is in part determined by the solid to fluid thermal conductivity ratio, K. In the case of a given wall to fluid temperature head variation, this ratio largely specifies the heat transfer distribution, driven by the nonisothermicity of the surface. In turn, the Biot number determines the rate of heat transfer and incorporates the flux reallocation effects. In both limiting cases, $\mathrm{Bi}\to\infty$ and $\mathrm{Bi}\to 0$, the conjugate problem degenerates. In other words, a low Biot number corresponds to a high convective thermal resistance, and thus a high temperature gradient in the fluid. Whereas in the case of a high Biot number, the largest temperature gradient will be in the solid and the wall temperature will be close to the fluid temperature. In either case, one of the thermal resistances is negligible, which concludes that the greatest conduction-convection coupling effect should be when both resistances are of the same magnitude, $\mathrm{Bi} \sim 1$.

The Biot number, used as a criterion to estimate the importance of conjugate analysis, can be presented in various suitable forms depending on the application. Alternative formulations, characterizing the body–fluid thermal resistances, include the Brun number $\mathrm{Br}_x = (d/x)\mathrm{K}^{-1}(\mathrm{Pr}\ \mathrm{Re}_x)^{1/3}$ [2], which gives a measure of the thermal resistances of the plate to that of the laminar boundary layer, and the conjugate Peclet number $\mathrm{Pe}^* = \mathrm{K}^{-1}\mathrm{Pe}^{1/3}$ [3], which is the ratio of the rate of advection by the flow to the rate of diffusion.

Conjugate Heat Transfer

The conjugate heat transfer problem considers the thermal interaction between a body and a fluid flowing over it, as a result of which a particular temperature distribution establishes on the interface. This temperature field determines the heat flux distribution, and thus the associated local heat transfer. Hence, from the perspective of the fluid, the properties of heat transfer of any conjugate problem are actually the same as its convective counterpart so long as an identical nonuniform temperature field could be imposed along the wetted surface. Thus, in general, the theory of conjugate heat transfer is in fact the theory of an arbitrary nonisothermal surface, but the temperature distribution on the interface is unknown a priori.

The problem of generally unknown temperature and heat flux distributions at the solid-fluid interface, determined by the coupled solution of the thermofluid dynamic equations in the fluid and the energy equation in the solid, is defined as conjugate heat transfer problem [4]. Fundamental analytical studies, utilizing incompressible laminar fluid flow along a flat plate which is uniformly heated at the external side, highlight the heat transfer dependence on thermal conductivity ratio [5,6]. Simplified expressions for the calculation of surface temperature, heat flux and Nusselt number, reduce the dependency to a function of the local Brun number, where Reynolds number is based on the free-stream velocity [7]. The critical proposed Brun number is in the order of 0.1; and for higher values, the results acquired by using conjugate and isothermal boundary conditions vary more than 5% [7].

Laminar flow inside a circular tube geometry was studied analytically [8] and numerically [9]. Axial conduction in the wall was found to lower the Nusselt number when compared to theoretical predictions in the absence of axial conduction, and to induce a heat redistribution effect. Specifically, a global 10% Nusselt number reduction, while local heat flux deviations up to 100%, is observed when the interface boundary condition is switched from iso-heat-flux (convective) to conjugate [9]. Moreover, when applying a constant heat flux to the external surface of the plate, the effect of wall conduction on the heat transfer augments with an increase of the solid-fluid thermal conductivity ratio (K) [8].

Due to the complexity of the conjugate problem, fundamental studies are commonly performed by numerical methods employing approximate solutions such as Green's functions [10,11]. Studies on a uniform shear laminar thin flat plate with varying thermal conductivity ratio, modeling the conjugate heat transfer from discrete rectangular heat sources, resulted in a relation where the Nusselt number is demonstrated to be a power function of the conjugate Peclet number [10]. The significance of solid conduction versus convection through the fluid was investigated, reporting low Peclet numbers to correspond to dominant conduction while Pe around 500 to indicate prevailing convection [10]. In the range of Pe from 5 to 500, the Nusselt number is reported to be up to 25% lower in the case of $K = 10$ (conjugate) compared to the adiabatic case of $K = 0$ (convective) [11].

Analytical studies on the laminar flow over a flat plate, which is heated at one side and insulated on the other side, have been carried out by Dorfman [12,13]. His findings highlight the role of temperature head gradients on local heat transfer. While increasing temperature heads (flow approaches from insulated side) corresponds to augmented heat transfer coefficients, the contrary case of decreasing temperature heads leads to lower than isothermal boundary condition heat transfer [13–15]. Moreover, for a surface at a temperature higher than the surrounding fluid, if the wall temperature increases in the flow direction (increasing temperature head), the descended layers of fluid at the adjoining wall come into contact with the increasingly hotter wall, yielding a local temperature augmentation within these layers. Consequentially, the cross-sectional temperature gradients near the wall turn out to be greater than in the case of constant wall temperature, which leads to higher than isothermal surface heat transfer coefficients. In contrast, for the case of decreasing surface temperature in the flow direction, the cross-sectional temperature gradients near the wall, along with the associated heat transfer coefficients, are less than those for an isothermal surface, and may become zero if the streamlined surface is sufficiently long [14]. In addition, it is important to note that the iso-heat flux boundary condition is a Nusselt number upper bound over the iso-thermal interface boundary condition. As a consequence, for a heated plate of increasing temperature head, all conjugate Nusselt number distributions must lay within the two cases [8]. Furthermore, in general, at increased levels of turbulence and for higher Reynolds and Prandtl numbers, the effect of nonisothermicity decreases monotonously [14].

A more specific numerical study focusing on the conjugate effects over the rib indicated that for Reynolds numbers below 2000 and $K=1$, the obstacle behaves as a thermal insulator for the air flow [16]. As the thermal conductivity ratio increases, by orders of magnitude, the variations in surface temperature decrease. On a similar investigation with $\mathrm{Pr}=0.71$, the change in thermal conductivity ratio from the isothermal case to the conjugate case of $K=1$ resulted in an average Nusselt number deviation of 32% [17].

Flow Over a Backward Facing Step

When the channel cross section is abruptly enlarged in the presence of a rib, the downstream turbulent flow exhibits a number of complex flow features such as reversal and recovery, turbulent mixing, regions of reattachment, and eventually redeveloping boundary layers.

The region of separated flow in the wake, between the back face and the reattachment line, is occupied by the recirculation region (in a time averaged sense). The exact location of reattachment, where the wall near flow initially begins to realign with the surface, is regarded as a key parameter for the separated flow. Experiments reported the near wall flow region to be substantially different from an ordinary boundary layer [18,19].

When the flow passes a rib obstacle, a free shear layer is formed at the sharp corner due to the interaction between the separated mainstream flow and the reverse flow in the recirculation region downstream. This free shear layer differs substantially from an ordinary mixing plane due to its high turbulence level [20], which also causes a gradual augmentation of its size at an increased distance from the rib [21]. In the region of flow reattachment, the separated shear layer curves sharply downward and impinges on the wall. When subjected to the effects of stabilizing curvature and a strong interaction with the wall, the shear layer is substantially split into two fractions [21,22]. Since the energy of the first part does not suffice to overcome the strong adverse pressure gradient, it is deflected upstream; being reversed, it forms the recirculating flow region. The second part of the shear layer is carried away downstream, and contributes to the growth of a new subboundary layer reattached to the wall [21].

In backward facing step studies, considering the effects of boundary layer states at separation (laminar/turbulent), there exists a sudden large elongation of the reattachment length from laminar to transitional flows, followed by a gradual decrease within the transitional regime. Toward fully turbulent flow, the dependency is observed to be much weaker [22–25]. In addition, an augmentation in free-stream turbulence level is reported to yield decreased reattachment lengths [23]. Moreover, as free-stream Reynolds number increases, an elongation of the separation region occurs, such that an augmentation of $\mathrm{Re}_{\mathrm{Dh}}$ from 200 to 2000 is observed to double the reattachment length [16].

Regarding heat transfer in backward-facing step geometries, the Nusselt number within the reattachment zone is controlled by the turbulence level near the wall. The local turbulence levels are augmented compared to an ordinary boundary layer, and in turn result in a proportionally larger Nusselt number [20]. Further downstream, a steady gradual Nusselt number decrease is observed and coincides with the growth of the thermal boundary layer following reattachment [26].

The direct relation of flow reattachment region with local heat transfer distribution has been extensively studied in literature. The local Nusselt number distribution is typically characterized by an initial increase within the separation bubble, followed by a peak in the vicinity of the reattachment region [20,27]. The maximum in the streamwise local Nusselt number profile, $x_{\max}$, has been considered a significant indication for the location of the reattachment point, $x_{R,}$ commonly defined by the change of sign in skin friction coefficient. However, in literature, there appears to be high inconsistency in the predicted relation between the locations of $x_{\max}$ and x_R [28]. While it is generally assumed that the locations of maximum heat transfer and reattachment coincide, this is an exceptional case [28].

Sparrow et al. [28] indicated that one of the major influences regarding the relationship between $x_{\max}$ and x_R is believed to depend on the separation bubble aspect ratio. With an increase in Reynolds number, a significant elongation of the separation bubble occurs, evidenced by experiments yielding to doubled reattachment length with Re augmentation from 200 to 2000 [16]. Furthermore, $x_{\max}$ is observed to be greater than x_R for short bubbles ($x_R/H<4$) and $x_{\max}<x_R$ for relatively long bubbles ($x_R/H>7$) [28]. This is supported by literature indicating laminar flows to mostly exhibit $x_{\max}>x_R$ [29], and turbulent experiments determining the location of maximum heat transfer coefficient to be upstream of the reattachment point [20,27,30]. Interestingly, for moderate bubble sizes, Sherwood and Nusselt numbers exhibited a double peak [27,31]. This appears to be consistent with the observed peaks in fluctuating wall shear component and turbulence intensity upstream and downstream of the reattachment [20,25,26]. In addition, conjugate numerical studies on backward-facing step flow indicated the peak in Nusselt number in the reattachment region to shift further downstream and increase in magnitude with increased thermal conductivity ratio [31].

Moreover, there have been significant efforts to relate the aerodynamic quantities with local heat transfer. Expressed in terms of the quantitative dependency between heat transfer and shear stress, the Reynolds Analogy presents a fundamental relationship for laminar boundary layers, relating Nusselt number linearly with skin friction coefficient and Reynolds number. Moreover, for certain specific applications, the Reynolds analogy is extended to more complex problems of turbulent flows. However, in the case of flow over a backward-facing step geometry, such an analogy is demonstrated to fail [32], to the extent that a maximum Stanton number may be at a point where skin-friction coefficient is zero [20]. Interestingly, a Stanton number relation to the fluctuations of the skin-friction coefficient, rather than the mean, is observed [26].

Experimental Facility

The experimental facility is the simplified model of a generic turbine internal cooling channel that is scaled up by a factor of 15. It consists of three pieces such as the inlet, test, and exit sections and each section has a cross-sectional dimension of 75×75 mm, with longitudinal dimensions of 1400 mm, 1260 mm, 800 mm, respectively. The inlet and exit sections of the channel are made of smooth flat walls, whereas one wall of the test section contains the ribbed perturbation elements, Fig. 2.

Upstream of the channel, a honeycomb with 3 mm cell size is used along with a NACA bellmouth to provide flow conditioning. In gas turbine cooling passages, even though the aerodynamic flow development initiates in the root section of the turbine airfoil, the part of the cooling passage which promotes heat exchange is the serpentine passages, modeled as the test section segment of the facility. Thus, the unheated aerodynamic development length in the inlet section provides further similarity with the real engine environment, Fig. 2. The flow downstream of the inlet duct is used as a reference point for calculating the Reynolds number, based on hydraulic diameter of the section and core flow velocity measured via Kiel-head probe. To better characterize the aerodynamic characteristics of the wind tunnel, dividing the square test section inlet into 3348 grid points, hotwire anemometry data are acquired at 100 kHz for one second duration at each point.

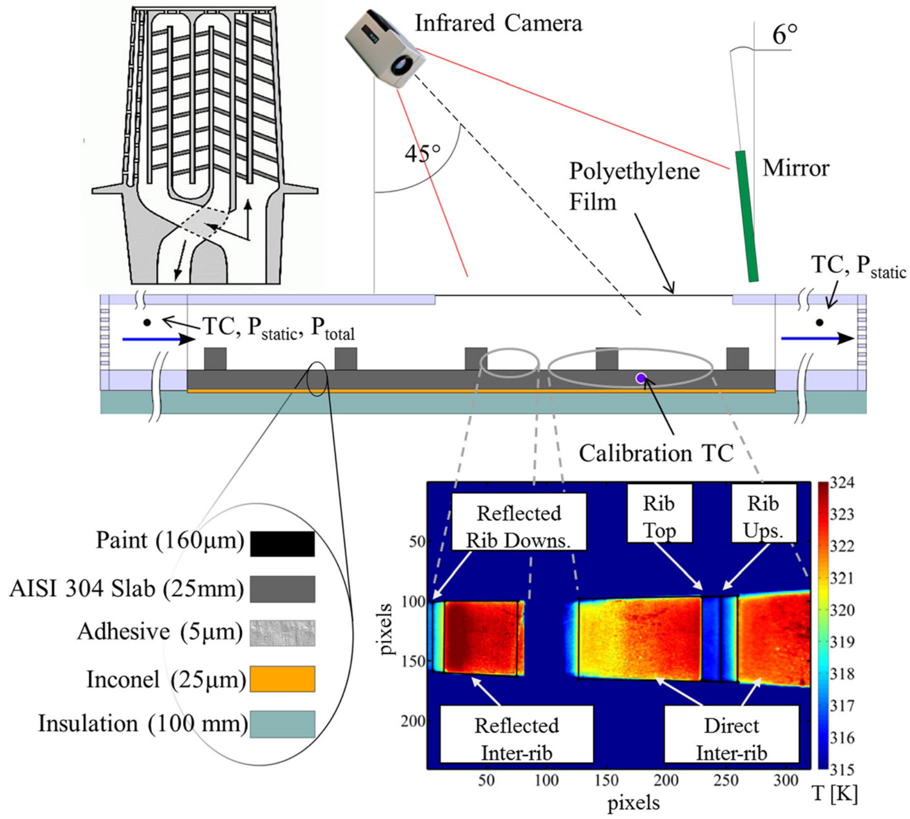

Fig. 2 Schematic of the experimental setup

The resulting mean turbulence intensity is computed to be 5%, whereas toward the channel centerline drops to 2%.

The geometric similarity is of fundamental importance in turbine cooling passages due to its major influence on local flow structures. In literature, there exist numerous alterations in parameters such as aspect ratio, blockage factor, rib pitch to height ratio, rib angle of attack, rib shape and profile, and number of ribbed channel walls. In this investigation, the square test section consists of two flat glass lateral walls, and a glass top wall with an optical access formed by a tensioned polyethylene film, at the base of which lies the 25 mm thick one-piece slab with turbulators. Made of a single AISI304 steel piece, it includes 6 square rib type perturbators yielding a blockage ratio of 30%, rib pitch to height ratio of 10, and rib angle of attack of 90 deg, Fig. 2.

The chosen configuration results in a particularly complex flow behavior with high levels of turbulence and a substantially three-dimensional flow character. From the perspective of aerodynamic similarity to engine conditions, experiments are conducted at $Re_{Dh} = 40{,}000$. For conjugate heat transfer considerations, engine representative Biot number and solid to fluid thermal conductivity ratio are used, 1 and 600, respectively. At such a high thermal conductivity ratio and Biot number in the order of unity, considering both thermal and convective resistances are of the same magnitude, the heat transfer dependence on thermal boundary condition (conjugate case) is amplified. Alternatively, considering the criteria outlined in Ref. [7], using the characteristic length associated with rib height, the local Brun number can be estimated as 0.17; greater than 0.1, the conduction-convection coupling effects are non-negligible.

The steel slab is painted black with uniform highly emissive layers of Nextel Primer 5523 and Nextel Suede Coating 428-26, by means of an airbrush. The black coating is matte, soft, and because of diffuse reflection, the surface is nondazzling. At the external side, the slab is heated by means of a 25 μm thick Inconel sheet which is powered by a 16 V–150 A DC power supply. The current is dissipated as thermal energy by the Joule effect and is conducted away by the parts in contact, Fig. 2. Inconel is known to provide uniform heat flux across the applied area and retains strength over a wide range of temperatures. The external side of the steel slab is equipped with 100 mm thick thermal insulation; considering the conservation of energy, the heat flux losses into the insulation can be estimated to be $\sim$0.7%.

For calibration and monitoring purposes, the slab is instrumented with 15 T-type thermocouples, held in place by Omega OB-101 thermally conductive, electrically insulating paste, applied to 3 mm holes drilled in the metallic slab at several locations along the channel. The thermocouples are located 0.5 mm away from the surface of the slab, and considering the local Biot number in the order of 10^{-3}, the temperatures measured at the thermocouple bead locations are equivalent to surface measurements.

The infrared measurements are conducted for the 4th pitch of the test section. In similar investigations, it has been demonstrated that the flow appears periodic starting with the 3rd rib pitch [33]. The Flir SC3000 infrared camera is located at 45 deg from the vertical; since the radiation exchange of surfaces are linearly proportional with the view factor, this configuration is selected to provide a good compromise for pixels on both the vertical and horizontal surfaces. The downstream face of the rib, along with the rib-shadowed portion of the inter-rib space is observed via a Newport 75K00ER3 mirror, featuring a reflectance in the order of 95% in the 8–9 μm range of the camera.

Experimental Methodology

The integrity of the infrared thermography measurements is highly dependent on an accurate calibration of the camera object signal against the test surface temperature. Considering the large difference in view factors of the direct and mirror reflected portions of the image, independent in-situ calibrations are performed via the slab embedded thermocouples. Such regional calibration techniques are based on the assumption that the slope of the calibration curve is constant for all the pixels, which enables the use of a single curve established at the reference. The local out of focus compensation, presenting itself as a bias shift among pixels, is corrected by a single image acquired at uniform ambient temperature.

The perspective distortions are corrected independently for each region of the sampled data by projection transformations, and are mapped onto a plane. The resolution of the transformed image is superficially augmented in each dimension through sub-pixel interpolation, resulting in a mean scale factor of 2.64 pixels/mm.

Furthermore, the acquired temperature results are ensured to reflect pitch to pitch temperature periodicity by linearly weighted averaging of overlap regions among 4th and 5th pitches. Finally, in order to reduce the noise content, a median filtering methodology is used; this is typical for applications where the goal is to simultaneously reduce peek noise and preserve edges. The temperature distribution across the channel is averaged with respect to the symmetry plane data followed by a Gaussian low pass filter to smooth out spuriously high gradients.

To acquire the surface heat flux distribution, a single generic pitch of the ribbed channel is modeled by COMSOL software. The boundary conditions for the numerical 3D conduction problem are uniform heat flux, in this case 1733 W/m^2, along the slab external surface, the measured temperature distribution on the wetted top surface, adiabatic lateral walls, and periodic boundary condition on the transverse direction where the solid, in reality, is interrupted, Fig. 3. The mesh consists of over 1.5×10^6 tetrahedral elements with a maximum body and surface element size of 1 mm and 0.1 mm, respectively.

Enhancement Factor Calculation From the infrared thermography measured surface temperatures, and the surface heat flux distributions obtained from COMSOL, it is possible to calculate the local heat transfer coefficient, $h(x,y) = q(x,y)/(T(x,y) - T_\infty)$, where T_∞ is the thermocouple measured air bulk temperature along the channel axis, experimentally verified to vary linearly from inlet to exit and considered as constant within a pitch. Subsequently, the computed heat transfer coefficient is nondimensionalized as Nusselt number, $\mathrm{Nu} = h(x,y)D_h/k_f$, where D_h is the channel hydraulic diameter and k_f is the thermal conductivity of air.

In order to quantitatively assess the impact of artificial roughness elements on internal cooling channel performance, and thus to determine the relative heat transfer enhancement, the Nusselt number is normalized with respect to an empirical heat transfer correlation, $\mathrm{EF} = \mathrm{Nu}(x,y)/\mathrm{Nu}_o$. The denominator is obtained from the Dittus-Boelter equation

$$\mathrm{Nu}_o = 0.023\mathrm{Re}_{\mathrm{Dh}}^{4/5}\mathrm{Pr}^{0.4} \quad (3)$$

a correlation for computing the local Nusselt number for hydrodynamically and thermally fully developed turbulent flows in smooth circular tubes, valid for $0.7 < \mathrm{Pr} < 160$, $\mathrm{Re}_{\mathrm{Dh}} > 10^4$, and $L/D_h > 10$.

Uncertainty Analysis. In the scope of this study, the heat transfer measurements have three sources of uncertainty resulting from independent contributions of the wall temperature, the COMSOL calculated surface heat flux and the free-stream air temperature. It is estimated with a single sample uncertainty analysis based on the method proposed by Kline and McClintock [34].

The overall uncertainty in wall temperature measurements can be decomposed into several contributing factors, such as the uncertainty associated with the calibration of thermocouples, the variation of object signal due to camera noise, the radiation emitted by the optical film medium, and the uncertainty introduced by the infrared image data reduction, as well as filtering and calibration curve fitting. The calibration of the T-type thermocouples is conducted in an oil bath by means of a thermometer with a resolution of 0.1 K over a range of 15 points. Including the effects of analog to digital discretization error, the thermocouple uncertainty is computed to be 0.18 K; the value is within the calibration curve's mean deviation from linearity (~0.15 K). The infrared camera object signal, a function of the spatial location and the surface temperature, varies on average by 3.2 intensity units among 30 consecutive images. Considering the calibration curve slope, it results in a camera noise associated temperature uncertainty of 0.06 K. The temperature difference on the polyethylene optical film during the calibration and the data acquisition is measured to be up to 1 K; and through experimental observation, the resulting object signal variation corresponds to 0.2 K slab temperature deviation. Another uncertainty contributor is the lateral temperature nonuniformity at a given camera calibration instance; estimated by the deviation of thermocouple readings in the lateral direction, its propagation to temperature-object signal relation is of the order 0.1 K. The contribution of raw infrared image filtering procedure to uncertainty is around 0.15 K. Lastly, the uncertainty introduced by the calibration curve fitting procedure is quantified as the deviation of the points from the second order polynomial fit (up to 0.12 K). Considering the above mentioned quantities, the cumulative infrared thermography wall temperature measurement accuracy is estimated to be ±0.35 K.

The heat flux at the wetted surface of the slab results from a numerical computation, where the boundary conditions consist of measured wall temperature and imposed slab external side heat-flux. Suitable for experimental uncertainty propagation into numerical models, Ref. [35] considers a deterministic perturbation approach to each of the physical independent quantities; the differences with the unperturbed solution provide an estimate on sensitivities. Perturbations in the external boundary heat-flux (prone to errors from voltage, current, and area measurements), along with uncertainty in infrared wall temperature, are observed to propagate and produce a cumulative surface heat flux uncertainty of 0.76%.

The local free-stream air temperature, $T_{\infty,}$ is computed from the thermocouples located at the inlet/exit cross sections of the facility. With additional sources of uncertainty provided by the deviation of the three readings among one another, the resulting cumulative air temperature uncertainty is 0.55 K.

Given the above calculated individual contributors, the cumulative expected uncertainty in heat transfer coefficient is estimated to be 3.4%. With the additions of air thermal conductivity and hydraulic diameter uncertainties, this translates into a Nusselt number uncertainty of 3.7%. Moreover, with the Reynolds number uncertainty of order ±3.3%, the subsequent enhancement factor accuracy is around ±4.5%.

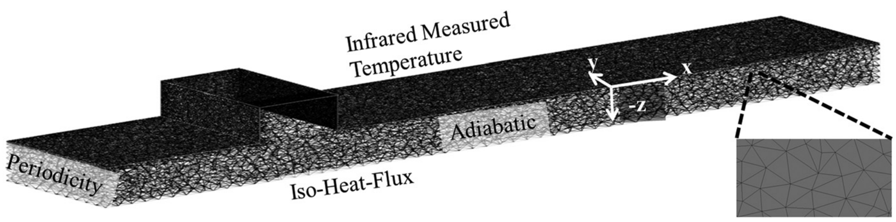

Fig. 3 Ribbed slab FEM model

Methodology Validation. In order to verify the experimental conjugate heat transfer measurement technique, as well as for conducting baseline investigations, an initial experiment is conducted on a flat plate geometry where uniform heat flux boundary condition is applied at the external side of the channel bottom wall. The wetted surface temperature distributions are acquired via infrared thermography; and, along with COMSOL acquired top surface heat flux, the heat transfer coefficient can be computed. The corresponding symmetry line average Nusselt number is 95.8, in good agreement with the circular tube Dittus-Boelter correlation which provides 96.4, Eq. (3).

For parallel turbulent flow over a fully turbulent, no pressure gradient flat plate, with fixed aero and thermal boundary layer shapes, the corresponding iso-heatflux and iso-thermal interface boundary condition Nusselt number correlations are [36]

$$\mathrm{Nu}_{x'} = 0.0308\mathrm{Re}_{x'}^{4/5}\mathrm{Pr}^{1/3} \tag{4}$$

and

$$\mathrm{Nu}_{x'} = 0.0296\mathrm{Re}_{x'}^{4/5}\mathrm{Pr}^{1/3} \tag{5}$$

In the test case, the flow starts developing further upstream of the heated section, i.e., the aerodynamic boundary layer starts developing prior to its thermal counter-part. Its effect on local Nusselt number is rectified by an unheated entry length correction [36]

$$\mathrm{Nu}_{x'\xi} = \mathrm{Nu}_{x'}/\left(1-\left(\xi/x'\right)^{9/10}\right)^{1/9} \tag{6}$$

where ξ is the unheated inlet section length and x' is the longitudinal dimension calculated locally from the inlet. Utilizing Eqs. (4) and (5) and by correcting for the unheated aerodynamic inlet length in Eq. (6), it is possible to acquire baseline Nusselt number distributions for purely convective heat transfer cases.

Figure 4 presents the experimental laterally averaged conjugate Nusselt number distribution with error bars, along with the theoretical cases where the interface boundary condition is iso-heatflux and isothermal. The longitudinal dimension is expressed as the local Reynolds number, with length scale (x) referenced to the heated slab leading edge. In all three cases, due to thermal boundary layer development, there is a monotonous decrease in Nusselt number at increased axial position.

In agreement with theory [8], the isothermal boundary condition case is a lower bound on heat transfer since, as the thermal boundary layer develops, the descended layers of fluid at the adjoining wall come into contact with closer solid temperatures, decreased temperature head, resulting in reduced heat flux. As less work is done on the local thermal boundary layer, the cross-sectional temperature gradients near the wall reduce in the downstream direction, yielding lower heat transfer. In contrast, for the iso-heatflux wetted boundary condition, an equal amount of work is inflicted on the thermal boundary layer, independent of local heat transfer coefficient.

In the conjugate case, in addition to the adverse effects of thermal boundary layer development on Nusselt number, the conduction within the solid has also an impact on local heat transfer. On one hand, the longitudinal conduction within the solid in the flow upstream direction (in this case characterized to be in the order of 2.5% of the bottom imposed value) ensures more than isothermal local heat flux. But, on the other hand, since the solid cannot sustain as large thermal gradients as the iso-heatflux boundary condition, the resultant conjugate heat transfer coefficient is less. As demonstrated in Fig. 4, within the uncertainty, the experimental conjugate results are in between the two limiting cases. Overall, the Nusselt number has low dependency on thermal boundary condition, of the order 3%; this is expected considering the turbulent flat plate flow at relatively high Reynolds number [14].

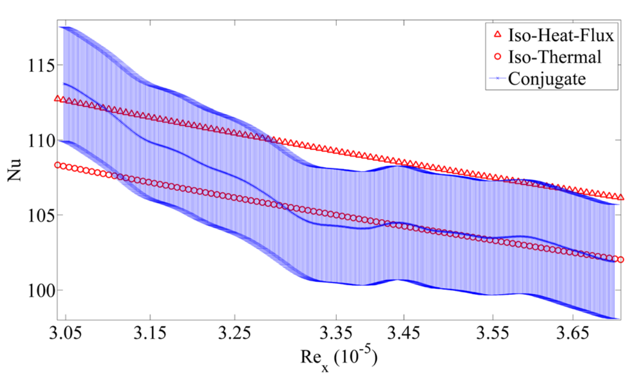

Fig. 4 Conjugate flat plate Nusselt number

Results

Rib Roughened Channel Mean Flow Field. As an overview, the mean flow field inside the rib-roughened cooling passage is presented by the complimentary PIV investigation, Fig. 5 [33].

Starting from an unperturbed state, as the fluid encounters the rib, it experiences a strong deviation imposed by the obstacle, forcing it to adapt to the decreased channel cross section. It is accelerated in order to pass the rib and subsequently experiences an expansion further downstream, as the cross sectional area abruptly increases following the backward face of the rib. The periodic behavior of the consecutive acceleration in the vicinity of the obstacle and the deceleration of the fluid in the inter-rib spacing is one of the most dominant aspects of the flow in rib-roughened channels. At the investigated Reynolds number, since

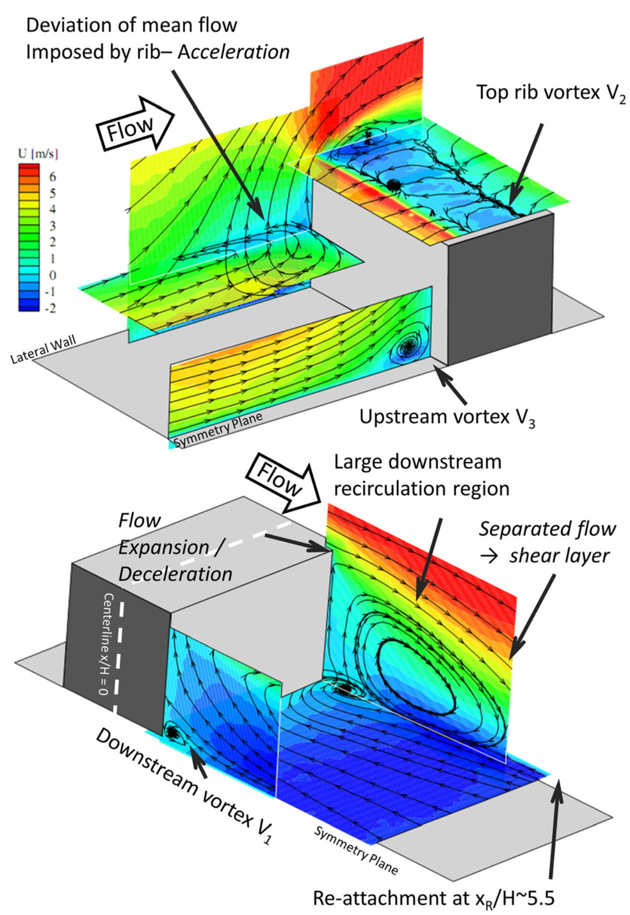

Fig. 5 Visualization of the ribbed channel flow field [33]

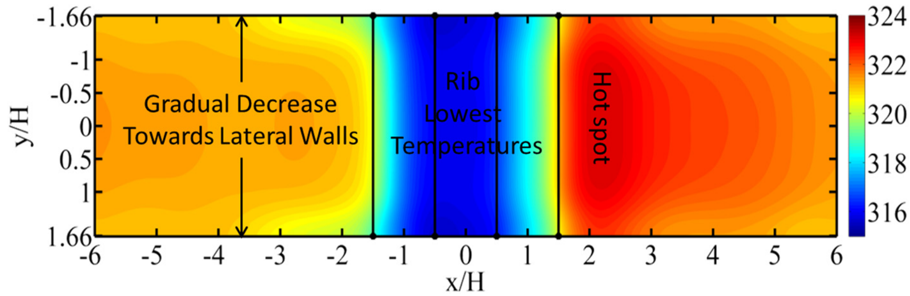

Fig. 6 Pitch temperature distribution (K)

the contribution of the inertial terms into fluid momentum balance is dominating, the flow is not able to follow the abrupt changes of the surface. It is the sudden enlargement of the channel downstream of the perturbator which causes the stream to separate from the surface, resulting in the recirculation region downstream, Fig. 5.

Apart from this recirculation region, the flow field exhibits a clockwise rotating separated flow region on top of the rib, V_2, as well as a small vortex cell V_1 in the downstream corner of the rib. Located within the rib wake, the V_1 vortex exhibits a counterclockwise rotary motion, opposing the mean angular velocity of the recirculation region. Toward the obstacle, the stream traces of V_1 and recirculation region coincide, such that the flow impinges onto the downstream surface of the rib. Similarly to V_2, the V_1 vortex cell occurs over the entire channel span.

Further downstream, the mean flow passes the rib and the subsequent recirculation zone, and at the reattachment region, there exists an impingement towards the channel bottom wall. In this case, defined by the change of sign in skin friction coefficient, the reattachment point is determined to be around $x/H \sim 5.5$ downstream of the rib center-plane. Once the flow reattaches, the boundary layer redevelops and grows within the inter-rib spacing, until the next turbulator. Immediately upstream of the rib, the stream strongly impinges on the vertical surface such that its vorticity and the repeatedly induced separation of the boundary layer give rise to the clockwise rotating vortex structure V_3 [33]. This effect is observed to be most dominant towards the symmetry plane. At the channel bottom wall, as the mean flow approaches the rib, a widthwise deflection occurs, indicated by the abrupt transverse flow motion. This pressure driven acceleration induces a region of high horizontal momentum, which is eventually captured by the mainstream flow and shed away downstream. As the flow crosses over to the next rib pitch, the described cyclic behavior of complex flow interactions perpetuates.

Local Temperature and Heat Flux Distributions. The IR measured projected surface temperature and its cross-sectional symmetry line distribution are presented in Figs. 6 and 7, where all dimensions are normalized by the rib height, H. Overall, it is evident that the lowest temperatures are measured in the vicinity of the rib. On the rib upstream facing wall, $-1.5 < x/H < -0.5$, there is a continuous decrease in temperature, followed by a relatively isothermal region on the rib top surface $|x/H| < 0.5$, Fig. 6. On the rib downstream face, $0.5 < x/H < 1.5$, the temperatures monotonously increase, and this trend continues in the beginning of the inter-rib space until $x/H = 2.2$, where the highest wall temperatures are observed, Fig. 7. Over the remaining inter-rib space, the temperature decreases monotonously in the streamwise direction, x/H from 2.2 to 6 and from -6 to -1.5. In the widthwise direction, toward the lateral walls, there exists a gradual decrease in temperature with respect to the symmetry plane, more significant in the $|y/H| > 1.3$ region.

By applying this temperature distribution as a boundary condition to COMSOL, it is possible to extract the local surface-normal heat flux. Figure 7 presents the symmetry line heat flux distribution, normalized by the uniform value imposed under the slab. The flux redistribution within the solid is evident, where on top of the rib up to 120% and in the downstream region as low as 10% of the bottom flux values are observed. Even though the global trend of lower temperatures implying higher surface heat extraction is valid, in various regions of the wetted surface, these effects are amplified or suppressed depending on local conduction.

In the rib upstream region, $-3.5 < x/H < -1.5$, it is possible to observe an almost uniform decrease in heat flux, where the temperature presents an initial plateau followed by a steep decrease, just upstream the rib edge. Similarly on the upstream face of the rib, $-1.5 < x/H < -0.5$, where the temperature presents a monotonous decrease, the heat flux is shown to reflect a sinusoidal behavior. On the rib top surface, toward the center, a heat flux peak is observed, otherwise not noted in the temperature contours. Similarly, even though the hottest spot in the temperature contours occurs at about $x/H = 2.2$, the minimum heat flux occurs at $x/H = 1.9$. These types of flux redistribution behavior are an artifact of the solid conduction, observed to be especially dominant in the vicinity of the rib which creates a local heat sink effect, Fig. 7. Overall, the temperature and flux distributions reflect a locally decoupled behavior, where the isothermal or iso-heat flux convective boundary condition cases would assume otherwise.

In conjugate heat transfer applications, a more global quantity which characterizes the effects caused by the existence of a noninsulating solid is the longitudinal heat flux, which quantifies the global axial conduction. For the present configuration, at all cross-sections within the inter-rib space which are at least $1.5H$ away from the rib, the ratio between the longitudinal heat flux and the imposed external side heat flux is in the order of $\sim$8%; with the maximum being $\sim$17% located toward the channel symmetry-line close to the wetted surface.

Heat Transfer Distributions and Aero-Thermal Interactions. Considering the characteristic flow patterns developing inside internal ribbed cooling channel geometries, the local heat transfer can be contrasted with the nearby flow structures. Figure 8 presents the local EF distribution, in addition to time-averaged PIV stream traces on the bottom wall, along with the

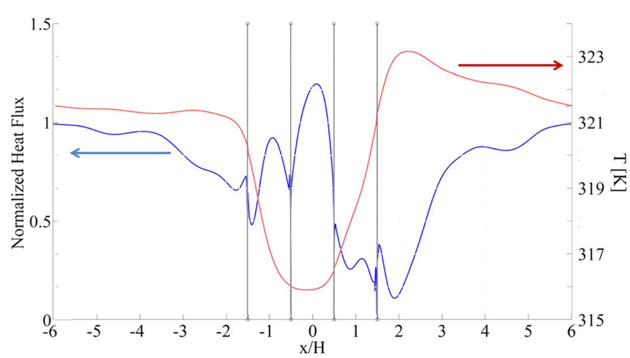

Fig. 7 Symmetry line temperature/normalized heat flux

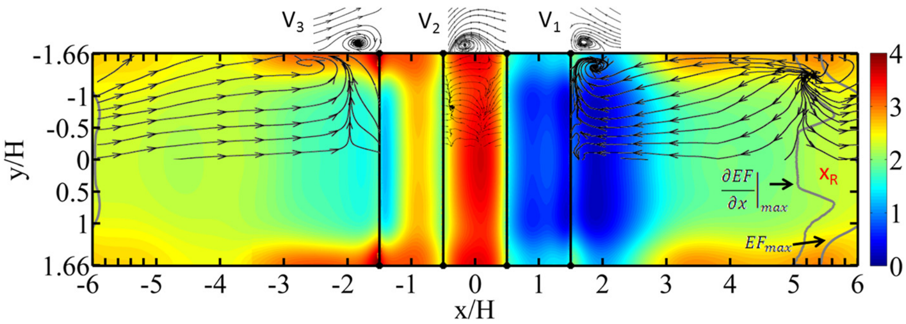

Fig. 8 Pitch enhancement factor distribution

symmetry plane V_3, V_2, and V_1 vortex structures located in front of, over, and behind the rib, respectively [33]. Moreover, the widthwise averaged EF chart can be found in Fig. 9.

The $-6 < x/H < -3.8$ region is the part of the ribbed channel where the flow is attached immediately downstream of the large separation region. Slight stream-wise decrease in enhancement factor is associated with the thermal boundary layer growth. On average, the significantly greater than flat plate EFs, EF $\sim 2.4 \gg 1$, is caused by the high levels of turbulence. Further downstream, for the region bounded by $-3.8 < x/H < -2.5$, the evident axial decrease in EF seems to be associated with the potential effect of the rib reducing the longitudinal component of the velocity, causing an adverse effect on the boundary layer growth. In the immediate vicinity of the rib, $-2.5 < x/H < -1.5$, the flow is dominated by the existence of the clockwise rotating corner vortex V_3. Because of the blockage, the cold mainstream fluid is deviated away from the bottom wall which prevents its contact with the heated surface, resulting in further reduced EFs, of the order 1.55.

In Fig. 8, the upstream face of the rib consists of the $-1.5 < x/H < -0.5$ region. Within the $-1.5 < x/H < -0.8$ domain, locally lower enhancement factors, EF $\sim$ 1.2–1.6, are associated with the regional insulation created by the V_3 flow structure. Around $x/H = -0.8$, a local peak in heat transfer is observed, EF ~ 2.6, a consequence of V_3 vortex downwash along with the mainstream flow impingement, consistent with the PIV data [33]. To a lesser extent, this vortex downwash can also be observed on the bottom wall, indicated by the local peak in EF at $-1.8 < x/H < -1.5$, Fig. 9. Toward the lateral wall, $-3.5 < x/H < -0.5$ $|y/H| > 1.3$, the flow field is subjected to pressure driven lateral acceleration of the rib impinging mainstream flow, where this high momentum region translates to locally augmented EFs, Fig. 8.

The top face of the rib, $|x/H| < 0.5$, is where the highest EFs are observed. This is caused by the reduction in effective flow area, in turn resulting in much higher momentum flow, generating a region of high heat transfer. In Fig. 9, the location of EF peak ($\sim$3.6) at $x/H = 0.15$, is consistent with the aerodynamic throat and the V_2 vortex.

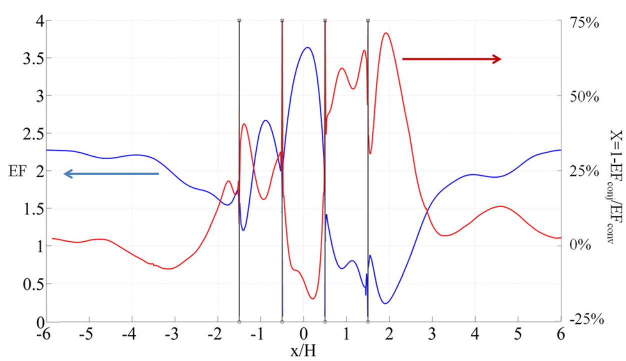

Fig. 9 Widthwise averaged EF and X distribution

The backward face of the rib, $0.5 < x/H < 1.5$, along with the immediate downstream area in the longitudinal direction, $1.5 < x/H < 2$, are the regions where the lowest EF values are observed, Fig. 8. This is caused by the large separation behind the rib, generating a local low momentum region with reversed flow, where the heat transfer is considerably less than in the rest of the passage. This is clearly observed by the sudden drop in EF for $0.5 < x/H < 0.9$, Fig. 9. In addition to the global separation, evidenced by the pitch minimum EFs of the order $\sim$0.5, the V_1 vortex further isolates the solid from the mainstream flow, observed both on the rib vertical and downstream walls, $0.9 < x/H < 1.5$ and $1.5 < x/H < 2$. The local peaks at $x/H = 1.2$ and $x/H = 1.6$ are caused by the impinging V_1 vortex downwash, although slightly, locally augmenting EF, Fig. 9.

Further away from the rib, $2 < x/H < 6$, the flow field is associated with the downstream recirculation bubble until the reattachment zone. Due to the increased penetration of the cool mainstream flow at increased axial position, the EF augments in the streamwise direction, Fig. 9.

Reattachment and Enhancement Factor. In Fig. 9, at around $x/H \sim 3.4$, prior to the aerodynamic reattachment point occurring at $x_R/H \sim 5.5$ [33], an unexpected peak in EF exists. Constituting only a local maximum, the reattachment associated global maximum occurs further downstream at $x/H \sim 6.01$. These findings are consistent with Ref. [28], since the recirculation bubble size is in between the criteria for long or short bubbles where the peak heat transfer is predominantly observed upstream and downstream of the reattachment point. The double peak reattachment heat transfer has already been observed in Refs. [27,31].

In Fig. 8, the reattachment region is estimated by the gray lines drawn in between $5 < x/H < 6.1$. The earlier line presents the local maximum in longitudinal derivative of enhancement factor. A strong positive gradient in EF, at a region bordering the large separation bubble, is indicative of the initialization of flow reattachment. If a reattachment point is to be selected, this would be the lower limit of the reattachment region. The gray line further downstream indicates the location of the longitudinal maximum in EF. For this geometry, since the rib downstream separation bubble is relatively narrow, and the global peak in heat transfer occurs after the reattachment point [28,32], thus the latter line is suggested to be an upper bound on the reattachment. Furthermore, analyzing the shape in the lateral direction, Fig. 8, it is observed that the re-attachment is earlier on the channel symmetry line. Toward the lateral walls, the location of the reattachment region initially increases until $y/H = 0.8$, followed by a decrease in reattachment length at the very edge of the channel, consistent with prior literature [27].

Role of Conduction in Convective Heat Transfer. Contrasting the findings of this conjugate investigation to analogous convective measurements with iso-heatflux wetted surface boundary condition [37], Table 1 presents the area averaged EFs for the different portions of the ribbed channel. In addition, quantifying

Table 1 Comparison with convective heat transfer

Boundary condition	Region averaged EFs						% Stand. Dev.	x_{max}
	Rib							
	Ups.	Top	Downs.	Mean	Inter rib	Pitch ave.		
Conjugate	2.34	2.99	0.86	2.07	2.01	2.02	36%	6.01
IsoHeatFlux	3.20	2.86	1.89	2.65	2.20	2.31	20%	5.45
X Deviation	27%	−5%	55%	26%	10%	14%	—	—

the nonuniformity with respect to the pitch mean value, percent standard deviations is computed. Furthermore, for the symmetry plane, reattachment associated maximum heat transfer locations, x_{max}, are also presented. Finally, to contrast the effect of a change in surface boundary condition, the conjugate EF deviation from the iso-heatflux case, $X = 1 - EF_{conj}/EF_{conv}$, is charted in Fig. 9, while the regionally averaged values are presented in Table 1.

In the conjugate case, the average EF on the upstream face is relatively high, 2.34, due the impingement of the mainstream flow on the surface. On the top face, the EF is even further augmented to 2.99, due to the local increase of momentum by the decrease in effective area. On the downstream face of the rib, the lowest average EF is observed, 0.86, caused by the large separation bubble behind the step. The rib, inter-rib, and pitch averaged EFs are 2.07, 2.01, and 2.02, respectively. Comparing the findings with the iso-heatflux surface boundary condition investigation, the variations in area averaged heat transfer coefficients are apparent, Table 1. This effect is specifically emphasized in the vicinity of the rib, $|x/H| < 3$, evidenced by the large deviation in EF from the iso-heatflux case, Fig. 9. This is believed to be attributed to the dominant conduction coupling, particularly observed around the rib as a result of closely distributed local heat sinks and sources. Particularly, with respect to the iso-heatflux investigation, the high solid thermal gradient yields to large differences in boundary layer thermal history.

More specifically, in the inter-rib space close to the rib, $-3 < x/H < -1.5$, the effect of conjugate boundary condition in EF can be as large as 22%, Fig. 9. On the rib upstream face, $-1.5 < x/H < -0.5$, the average deviation is 27%, and locally can be up to 41% at $x/H = -1.4$, where the V_3 vortex is dominant. The vortex creates an isolated region where the flow impinges on the side of the rib $x/H \sim -0.8$, being heated up, moves toward the bottom wall with reversed flow. Due to the increase in bulk flow temperature, and local decrease in wall temperature, Fig. 7, the temperature head reduces in the flow direction. Consistent with the fundamental conjugate heat transfer theory [14], a decrease in temperature head in the flow direction results in lower than convective EFs, further augmenting X at $x/H = -1.4$.

Over the rib top surface, the effect of the thermal boundary condition seems to have diminished to 5% globally, Table 1. Within this region, due to the aerodynamic throat, the local momentum is greatly augmented which results in high heat transfer coefficients, but as a consequence the dependency on thermal boundary condition is relatively low [14]. Additionally, in the presence of conduction within the rib, the top surface is a heat sink, as it is surrounded by much lower EF regions. This effect may explain the slightly higher conjugate EFs observed toward the rib centerline with respect to the iso-heatflux case, Fig. 9.

Downstream of the rib, $0.5 < x/H < 3$, the convective case overestimates the EF in the order of 55% and 70% on the rib downstream face and on the near bottom wall, respectively. Such large values are consistent for regions of lower momentum and decreased turbulence levels, where the thermal boundary condition selection has a much more dominant effect on heat transfer [14]. In Fig. 7, this is the portion of the pitch where only ∼20% of the bottom heat flux reaches the surface, resulting in much lower local thermal gradients than the iso-heatflux case, and thus reduced conjugate heat transfer.

Further downstream, for the conjugate boundary condition measurement, it has been observed that the peak heat transfer occurs at $x/H = 6.01$, roughly $0.5\,H$ downstream of the convective case. These findings are consistent with literature indicating an upstream shift in peak reattachment Nusselt number location with decreased thermal conductivity ratio, at the limit being purely convective [31].

Considering the global trends in Fig. 9, for a low conjugate EF region, the local work input to the flow is higher for the convective case since equal amounts of heat flux are imposed on the boundary layer independently of the local heat transfer coefficient. This could imply that under these circumstances the surface boundary layer will have a stronger gradient in the convective case than in the conjugate case, creating higher convective EF regions as seen in $0.5 < |x/H| < 3$, Fig. 9. On the contrary, for a region of high conjugate EF, the heat flux input to the fluid is higher than the iso-heatflux case. With a similar argument, it is possible to deduce that these regions will have lower convective EF values, e.g., rib top, in agreement with Ref. [8]. Consequently, a more nonuniform conjugate heat transfer distribution is maintained across the domain, where the percent EF standard deviation is 36% in contrast to the convective case which is 20%, Table 1.

Furthermore, comparing the pitch averaged EFs, the case study with iso-heatflux boundary condition results in a mean EF of 2.31, an over-prediction of the global heat transfer by 14%. To provide a sense of scale to the repercussions associated with such an error, the findings can be extrapolated to the real engine environment by assuming a self-similar internal turbine cooling channel where the compressor air coolant temperature is 900 K and the blade temperature is at the material limit, which is around 1200 K. Considering identical heat fluxes for both convective and conjugate boundary condition cases, if the interface boundary condition is set to iso-heatflux, which is unrealistic, then the predicted blade temperature reduces to 1163 K. Although miscalculation of blade bulk temperature by 37 K, may seem like a relatively small error, underestimations of metal temperature, as little as 30 K, are reported to reduce the life cycle of blades by half [38]. In turbine applications, when the blade temperature exceeds detrimental limits, thermal stresses become excessive and affect the structural integrity; blade life decreases, possibly resulting in thermal failure. Therefore, it is critical to predict accurately the local heat transfer coefficient as well as the local blade temperature to prevent local hot spots and increase turbine blade life. Alternatively, by models accounting for the conjugate nature of the heat transfer interaction, the engine designers may choose to decrease the safety factor and maintain the same blade temperatures. This would reduce the required coolant flow, and thus improve on the turbine efficiency, resulting in lower fuel costs for the same power output.

Conclusion

By infrared thermography surface temperature measurements, and via finite element energy balance within the solid, an experimental conjugate heat transfer investigation is conducted for a rib-roughened internal cooling channel geometry. The enhancement factor trends are compared with the basic flow features. For the attached flow immediately downstream of the large separation region, associated with the boundary layer growth, a slight overall decrease in enhancement factor is observed. In the immediate vicinity of the rib upstream face, the aero-thermal distribution is dominated by the existence of the clockwise rotating corner vortex V_3. The top face of the rib is where the overall highest EFs, and lowest temperatures, are observed, an artifact of reduction is effective area. The rib downstream region, until reattachment, is where the lowest EF values are observed, caused by the large time-averaged separation bubble in the wake of the rib. In the reattachment zone, a double peak in enhancement factor is reported, consistent with the size of the recirculation bubble. The initial smaller peak is located prior to and the second global maximum in enhancement factor is observed after the reattachment point.

More globally, the heat flux redistribution within the solid is demonstrated, locally in the order of 20% surplus on top of the rib and 90% deficit on the rib downstream bottom wall. Even though the global trend of lower temperatures implying higher surface heat extraction is observed to be valid, in various regions of the wetted surface, these effects are amplified or suppressed depending on local conduction, especially visible around the rib. Moreover, on the inter-rib spacing, the axial conduction is computed to be as high 17%. When compared with the convective iso-heatflux boundary condition findings, the effects of imposing the conjugate boundary condition result in mean deviations of 26%, 10%, and 14% over the rib, inter-rib space, and on the entirety of the pitch. Locally, this effect can be enhanced up to 70% in the rib downstream separation region. Moreover, when the surface boundary condition is switched from convective to conjugate, a half rib height downstream shift of reattachment associated peak heat transfer is observed.

In conclusion, the findings clearly indicate that accounting for the *true* thermal history of the flow, and in turn modeling the solid conduction in such high gradient convective heat transfer surfaces is crucial. In the specific case of the turbine cooling application, switching the thermal boundary condition from conjugate to iso-heat-flux resulted in a projected blade surface temperature reduction of 37 K in the engine environment. The underestimation of blade bulk metal temperature by 30 K is reported to reduce the life cycle of blades by half. For unbiased results, studies of such applications should respect the correct similarity parameters, i.e. reproducing the correct thermal boundary conditions.

Acknowledgment

The authors acknowledge the financial support of the Air Force Office of Scientific Research (AFOSR), Grant No. FA8655-08-1-3048, supervised by Dr. S. Surampudi and Dr. G. Abate of the European Office of Aerospace Research and Development.

Nomenclature

- Bi = $h\, d/k_s$ (Biot number)
- d = slab thickness
- D_h = channel hydraulic diameter
- Ec = Eckert number
- EF = Nu/$\mathrm{Nu_o}$ (enhancement factor)
- h = $q/\Delta T$ (heat transfer coefficient)
- H = rib height
- k = thermal conductivity
- K = k_s/k_f
- Nu = $h\, D_h/k_f$ (Nusselt Number)
- $\mathrm{Nu_o}$ = $0.023\mathrm{Re_{Dh}}^{4/5}\mathrm{Pr}^{0.4}$ (Dittus Boelter corr.)
- PIV = particle image velocimetry
- Pr = Prandtl number
- $\mathrm{Re_{Dh}}$ = $\rho \mathrm{V} D_h/\mu$ (Reynolds number)
- T = temperature
- ΔT = $T_{\mathrm{wall}} - T_\infty$ (temperature head)
- TC = thermocouple
- x = longitudinal distance (reference from rib center-plane or heated slab leading edge)
- x' = longitudinal distance from inlet
- x_R = reattachment distance
- $x_{\max}$ = maximum Nusselt number location
- X = $1 - \mathrm{EF_{conj}}/\mathrm{EF_{conv}}$
- y = lateral distance

Subscripts

- conj = conjugate boundary condition
- conv = convective boundary condition
- f = fluid
- s = solid
- ∞ = free-stream

References

[1] Kay, J. M., and Nedderman, R. M., 1985, *Fluid Mechanics and Transfer Processes*, Cambridge University Press, Cambridge, UK.
[2] Luikov, A. V., 1974, "Conjugate Convective Heat Transfer Problems," Int. J. Heat Mass Transfer, **17**(2), pp. 257–265.
[3] Cole, K. D., 1997, "Conjugate Heat Transfer From a Small Heated Strip," Int. J. Heat Mass Transfer, **40**(11), pp. 2709–2719.
[4] Perelman, L. T., 1961, "On Conjugated Problems of Heat Transfer," Int. J. Heat Mass Transfer, **3**(4), pp. 293–303.
[5] Luikov, A. V., and Aleksachenko, V. A., 1971, "Analytical Methods of Solution of Conjugated Problems in Convective Heat Transfer," Int. J. Heat Mass Transfer, **14**(8), pp. 1047–1056.
[6] Pozzi, A., Quaranta, G., and Tognaccini, R., 2008, "A Self-Similar Unsteady Flow With Conjugated Heat Transfer," Int. J. Heat Mass Transfer, **51**(7–8), pp. 1804–1809.
[7] Mosaad, M., 1999, "Laminar Forced Convection Conjugate Heat Transfer Over a Flat Plate," Int. J. Heat Mass Transfer, **35**(5), pp. 371–375.
[8] Mori, S., Sakakibara, M., and Tanimoto, A., 1974, "Steady Heat Transfer to Laminar Flow in a Circular Tube With Conduction in the Tube Wall," Heat Transfer-Jpn. Res., **3**(2), pp. 37–46.
[9] Barozzi, G. S., and Pagliarini, G., 1985, "A Method to Solve Conjugate Heat Transfer problems: the Case of Fully Developed Laminar Flow in a Pipe," ASME J. Heat Transfer, **107**(1), pp. 77–83.
[10] Li, Y., and Ortega, A., 1998, "Forced Convection From a Rectangular Heat Source in Uniform Shear Flow: The Conjugate Peclet Number in the Thin Plate Limit," Intersociety Conference on Thermal Phenomena, May, Seattle, WA.
[11] Ortega, A., and Ramanathan, S., 2003, "On the Use of Point Source Solutions for Forced Air Cooling of Electronic Components—Part II: Conjugate Forced Convection From a Discrete Rectangular Source on a Thin Conducting Plate," ASME J. Electron. Packag., **125**(2), pp. 235–243.
[12] Dorfman, A., 1982, *Heat Transfer for Flow Past Non-Isothermal Bodies*, Izd. Mashinostroenie, Moscow.
[13] Dorfman, A., 1985, "A New Type of Boundary Condition in Convective Heat Transfer Problems," Int. J. Heat Mass Transfer, **28**(6), pp. 1197–1203.
[14] Dorfman, A., 2009, *Conjugate Problems in Convective Heat Transfer*, Taylor & Francis, London.
[15] Dorfman, A., 1971, "Exact Solution of Thermal Boundary Layer Equation With Arbitrary Temperature Distribution on Streamlined Surface," High Temp., **8**(5), pp. 955–963.
[16] Young, T. J., and Vafai, K., 1998, "Convective Cooling of a Heated Obstacle in a Channel," Int. J. Heat Mass Transfer, **41**(20), pp. 3131–3148.
[17] Kanna, P. R., and Das, M. K., 2006, "Conjugate Heat Transfer Study of Backward-Facing Step Flow—A Benchmark Problem," Int. J. Heat Mass Transfer, **49**(21–22), pp. 3929–3941.
[18] Simpson, R. L., 1983, "A Model for the Backflow Mean Velocity Profile," AIAA J., **21**(1), pp. 142–143.
[19] Westphal, R. V., Eaton, J. K., and Johnston, J. P., 1981, "A New Probe for Measurement of Velocity and Wall Shear Stress in Unsteady, Reversing Flow," ASME J. Fluids Eng., **102**(2), pp. 478–482.
[20] Vogel, J. C., and Eaton, J. K., 1985, "Combined Heat Transfer and Fluid Dynamic Measurements Downstream of a Backward-Facing Step," ASME J. Heat Transfer, **107**, pp. 922–929.
[21] Zukauskas, V. A., and Pedisius, K. A., 1987, "Heat Transfer to Reattached Fluid Flow Downstream of a Fence," Wärme- und Stoffübertagung, **21**(2–3), pp. 125–131.
[22] Eaton, J. K., and Johnston, J. P., 1981, "A Review of Research on Subsonic Turbulent Flow Reattachment," AIAA J., **19**(9), pp. 1093–1100.
[23] Eaton, J. K., Johnston, J. P., and Jeans, A. H., 1979, "Measurements in Reattaching Turbulent Shear Layer," Proceedings 2nd Symposium on Turbulent Shear Flows, London.
[24] Armaly, B. F., Durst, F., and Pereira, J. C. F., 1983, "Experimental and Theoretical Investigation of Backward-Facing Step Flow," J. Fluid Mech., **127**, pp. 473–496.
[25] Adams, E. W., and Johnston, J. P., 1988, "Effects of Separating Shear Layer on the Reattachment Flow Structure Part 2: Reattachment Length and Wall Shear Stress," Exp. Fluids, **6**, pp. 493–499.
[26] Avancha, R. V. R., and Pletcher, R. H., 2002, "Large Eddy Simulation of the Turbulent Flow Past a Backward-Facing Step With Heat Transfer and Property Variations," Int. J. Heat Fluid Flow, **23**, pp. 601–614.
[27] Armaly, B. F., Durst, F., and Kottke, V., 1981, "Momentum, Heat, and Mass Transfer in Backward-Facing Step Flows," Proceedings of 3rd Symposium on Turbulent Shear Flows, Davis, CA.

[28] Sparrow, E. M., Kang, S. S., and Chuck, W., 1987, "Relation Between the Points of Flow Reattachment and Maximum Heat Transfer for Regions of Flow Separation," Int. J. Heat Mass Transfer, **30**(7), pp. 1237–1246.
[29] Aung, W., 1983, "An Experimental Study on Laminar Heat Transfer Downstream of Backsteps," ASME J. Heat Transfer, **105**(4), pp. 823–829.
[30] Seban, R. A., Emery, A., and Levy, A., 1959, "Heat Transfer to Separated and Reattached Subsonic Turbulent Flows Obtained Downstream of a Surface Step," J. Aerosp. Sci., **28**, pp. 809–814.
[31] Kanna, P. R., and Das, M. K., 2007, "Conjugate Heat Transfer Study of a Two-Dimensional Laminar Incompressible Wall Jet Over a Backward-Facing Step," ASME J. Heat Transfer, **129**(2), pp. 220–229.
[32] Jourdain, C., Escriva, X., and Giovannini, A., 1997, "Unsteady Fow Events and Mechanisms Leading to Heat Transfer Enhancement in a Ribbed Channel," Proceedings Eurotherm Seminar 55: Heat Transfer in Single Phase Flow.
[33] Casarsa, L., and Arts, T., 2005, "Experimental Investigation of the Aerothermal Performance of a High Blockage Rib-Roughened Cooling Channel," ASME J. Turbomach., **127**(3), pp. 580–588.
[34] Kline, S. J., and McClintock, F. A., 1953, "Describing Uncertainties in Single-Sample Experiments," J. Mech. Eng., **75**, pp. 3–8.
[35] Rabin, Y., 2003, "A General Model for the Propagation of Uncertainty in Measurements Into Heat Transfer Simulations and Its Application to Cryosurgery," Cryobiology, **46**, pp. 109–120.
[36] Kays, W. M., Crawford, M. E., and Weigand, B., 2005, *Convective Heat and Mass Transfer*, McGraw-Hill, New York.
[37] Cukurel, B., Selcan, C., and Arts, T., 2012, "Film Cooling Extraction Effects on the Aero-thermal Characteristics of Rib Roughened Cooling Channel Flow," ASME GT2012-68680.
[38] Han, J. C., 2006, "Turbine Blade Cooling Studies at Texas A&M University: 1980–2004," J. Thermophys. Heat Transfer, **20**(2), pp. 161–187.